

## Arcs and Clumps in the Uranian $\lambda$ Ring

Mark R. Showalter\*

Careful reprocessing of the Voyager images reveals that the Uranian  $\lambda$  ring has marked longitudinal variations in brightness comparable in magnitude to those in Saturn's F ring and Neptune's Adams ring. The ring's variations show a dominant five-cycle (72-degree) periodicity, although additional structure down to scales of about 0.5 degree is also present. The ring's shape is defined by a small overall eccentricity plus a six-cycle (60-degree) sinusoidal variation of radial amplitude around 4 kilometers. Both of these properties can be explained by the resonant perturbations of a moon at a semimajor axis of 56,479 kilometers, but no known moon orbits at this location. Unfortunately, the mass required suggests that such a body should have been imaged by Voyager.

The  $\lambda$  ring (1986U1R) was the first ring to be discovered during the Voyager 2 encounter with Uranus in January 1986. This narrow ring first appeared in a sequence of images acquired by the narrow-angle camera shortly before Voyager's closest approach to the planet (1). The ring falls roughly halfway between the  $\epsilon$  and  $\delta$  rings and is substantially fainter than any of the nine rings known previously. The  $\lambda$  ring was also detected in the Voyager photopolarimeter (PPS) and ultraviolet spectrometer profiles as the rings occulted the star  $\sigma$  Sgr (2, 3). These profiles have much finer radial resolution than the images,  $\sim 10$  m for the PPS; they indicate that the ring falls at orbital radius 50,024 km (4), a mere 272 km outside the orbit of the moon Cordelia (5). The optical depth  $\tau \approx 0.1$  for most of the ring's width ( $\sim 2$  km), but at finest resolution, the ring shows a central peak  $\sim 0.5$  km wide with  $\tau \approx 0.5$ . The ring was not detected by the analogous radio science occultation experiment (6). Subsequently, investigators have reexamined some of the most sensitive Earth-based stellar occultation data, but no definitive detections have been reported (7, 8).

The ring is visible in only a handful of Voyager images, and severe contrast enhancement is required in most of these. However, pixel averaging techniques improve the ring's detectability considerably (9, 10) and bring out some unusual properties from the noise (11, 12). Figure 1 shows profiles from two comparable images. The ring is apparent in the first image but is absent from the second, indicating that it is very variable. The profiles show  $\mu I/F$  versus orbital radius, where  $I$  is the reflected intensity and  $\pi F$  is the incident solar flux density;  $I/F$  is dimensionless and equals unity for sunlight illuminating a perfectly diffusing ("Lambert") surface at normal inci-

dence. The factor of  $\mu$ , the cosine of the emission angle, corrects for the variations in brightness with emission angle for a ring that is optically thin. To better quantify the  $\lambda$  ring's variations, we measured the ring's total reflected light by the "equivalent width"  $W \equiv \int (\mu I/F) dr$ , where  $r$  is the distance from the planet center. If the limits of the integral encompass the ring's full radial width in the image, then  $W$  is independent of resolution and smear (9, 10).

To map out the ring's brightness variations, one must assume the angular rate or "pattern speed" at which the variations propagate. The orbital mean motion  $n$  is the most plausible choice; the arcs in Neptune's Adams ring also propagate at this rate (13). The gravity model of Uranus (4) implies  $n = 1065.75^\circ$  per day for the  $\lambda$  ring. Figure 2 shows  $W$  measured from every suitable image in two Voyager sequences, plotted in this corotating frame. Aside from a correction for the ring's phase curve (12), the measurements are highly correlated, confirming that the pattern speed equals the ring's mean motion  $n$ . However, the coarse angular resolution and the short time baseline of only 2.3 days (6.8 rotations) imply that any pattern speed within 1% of  $n$  could be compatible with the data.

This longitudinal profile reveals a striking five-cycle periodicity. The amplitude of the periodicity is quite large, with the faintest regions  $\leq 10\%$  as bright as the ring's overall mean. The ring might be better described as a set of five arcs spaced by  $\sim 72^\circ$ ; in a Fourier series expansion of the data (Fig. 3), the fifth coefficient stands out above the others at a significance level of  $8\sigma$  to  $9\sigma$ . However, many other harmonics are present with amplitudes of up to  $4\sigma$ , showing that the arc structure is not sinusoidal. These deviations from a sinusoid are visible in Fig. 2; for example, the expected minimum near longitude  $300^\circ$  is rather subdued, and the transition from a maximum to a minimum at longitude  $350^\circ$  is particularly abrupt.

Because of the large-scale longitudinal

averages used, it is impossible to detect  $\lambda$  ring variations on scales smaller than about  $10^\circ$ . For that purpose, images with much higher intrinsic signal-to-noise ratio are required. Only two images fit this requirement, 26852.14 and 26852.19 (Fig. 4). They were taken by Voyager's wide-angle camera at an especially high phase angle  $\alpha = 172^\circ$ , where the ring's dust is highlighted. Image 26852.19 is a long exposure (96 s) that first revealed the faint Uranian dust belts (1), but the substantial smear makes it impossible to identify small-scale longitudinal features here [a larger scale trend did lead to some earlier speculations about the ring's variations (14)]. However, image 26852.14 is a much shorter exposure (1.92 s) that captured the same field of view without smear. The image shows  $15^\circ$  of the ring and, with contrast enhancement, reveals a distinct clump  $\sim 0.5^\circ$  long where the ring brightens by a factor of about 3.

Several Uranian rings have nonzero eccentricities and other radial oscillation modes (4), so it is worth examining the shape of the  $\lambda$  ring. The radial profiles (Fig. 1) give the ring's location to accuracies of  $\approx 5$  km. In the inbound image sequence, the other major rings provide reliable reference points; the outbound sequence has not been used because the major rings are invisible, and so the radial scale is less certain. Figure 5A shows the  $\lambda$  ring's radial position relative to a circle in each inbound image where it could be detected reliably. The longitudes refer to a frame rotating at the local apsidal precession rate, in which an

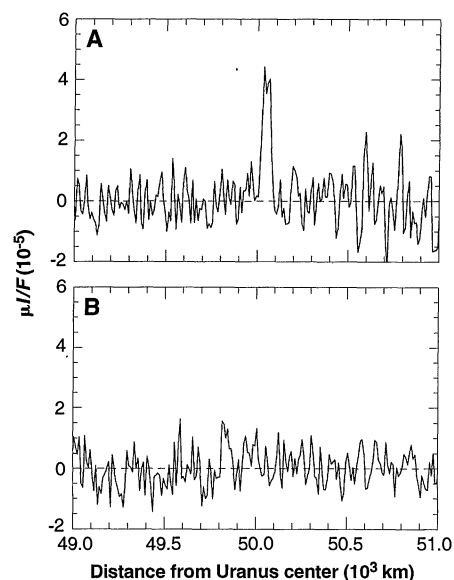


Fig. 1. Two radial profiles of the  $\lambda$  ring, based on extensive pixel averaging. The ring is plainly visible in image 26824.14 (A) but is completely undetectable in image 26823.50 (B). The two images are equivalent in overall quality. The processing behind these profiles is described in (22).

Center for Radar Astronomy, Stanford University, Stanford, CA 94305, USA.

\*Contact address: Mail Stop 245-3, NASA Ames Research Center, Moffett Field, CA 94035-1000, USA. E-mail: showalter@ringside.arc.nasa.gov

eccentric ring would have a fixed orientation. The best-fit ellipse has semimajor axis  $a = 50,024.6 \pm 0.7$  km and eccentricity  $e = (3.1 \pm 1.6) \times 10^{-5}$  but represents a very poor fit to the measurements. Using  $\chi^2$  statistics, a Keplerian ellipse can be ruled out with 99.8% confidence.

To test for the presence of another radial mode, I fit the data to a shape model comprising one mode with periodicity  $m$  plus a freely precessing ellipse ( $m = 1$ ). The assumed pattern speed of the extra mode was defined by the requirement that individual particles travel on Keplerian orbits. I have tested models with  $|m| \leq 20$ ; higher  $m$  values cannot be detected because measurements are averages over  $\sim 10^\circ$  of longitude. Negative  $m$  corresponds to pattern speeds faster than the mean motion; positive  $m$  corresponds to slower speeds. Of these modes,  $m = 6$  provides a very successful fit to the data (Fig. 5B). To assess the likelihood that this fit arose merely by chance, I generated 10,000 hypothetical data sets in which the radial measurements were identical but the corresponding longitudes were randomized. When I applied the same fitting procedure, only 4% of the randomized data sets yielded a similar quality of fit for any mode in the range considered. Hence, our confidence that the  $m = 6$  pattern did not arise by chance is 96%.

As a further test of the shape model, the ring's location in the two PPS occultation cuts was added for a final fit (Fig. 5C). The residuals increased slightly but remained reasonable in spite of the much smaller uncertainties ( $\sim 0.3$  km) in the PPS locations. According to the statistical tests, we

still have 89% confidence that this pattern did not arise by chance. The best-fit  $m = 6$  radial pattern has amplitude  $4.2 \pm 0.9$  km,  $a = 50,026.3 \pm 0.6$  km, and  $e = (2.8 \pm 1.2) \times 10^{-5}$  ( $ae = 1.4 \pm 0.6$  km).

The  $\lambda$  ring's variations are difficult to explain. Assuming a 2-km radial width, the  $\sim 72^\circ$  arcs should shear out in 3 years and the  $0.5^\circ$  clump in a mere 8 days. Clearly, a confinement mechanism is needed. Only a few other rings have shown comparable variations; Neptune's Adams ring and Saturn's F ring and Encke Gap ringlets are the prime examples. In each of these cases, gravitational perturbations by nearby moons are likely to be involved (13, 15, 16).

Corotation resonances (CRs) have been proposed as an explanation for other brightness variations in narrow rings (17). A ring is in corotation resonance if a perturbing satellite executes a whole number  $m_C$  of radial (eccentric) or vertical (inclined) oscillations per synodic period. Then the satellite's perturbations can induce ring particles to librate about  $m_C$  uniformly spaced corotation sites for an eccentric satellite or  $2m_C$  sites for an inclined satellite (18) (an eccentric satellite has one close passage to the ring per orbital period, whereas an inclined satellite has two). Because of the  $72^\circ$  periodicity observed in the  $\lambda$  ring, it is tempting to associate it with the  $m_C = 5$  corotation eccentricity resonance (CER) of a moon; the odd number excludes the possibility that an inclination resonance (CIR) plays a role. Such a moon would have to fall at one of two possible semimajor axes: 43,131.6 or 56,479.5 km. Unfortunately, no

moon has been detected at either location.

The ring's radial mode, on the other hand, is suggestive of the effects of a Lindblad resonance (LR), which occurs where a ring particle executes a whole number  $m_L$  of radial oscillations between successive encounters with a moon; here the moon's perturbations add in phase, leading to an  $m_L$ -lobed radial distortion that propagates around the ring at the moon's mean motion. In practice, LRs and CRs fall very close to one another, with  $m_L = m_C + 1$  for a moon's inner resonances and  $m_L = m_C - 1$  for its outer ones. The nearby LR also plays a crucial role in stabilizing the CR-induced librations (17, 18). Note, therefore, that a hypothetical moon at semimajor axis 56,479.5 km would have its inner CER atop the  $\lambda$  ring and would also have its inner  $m_L = 6$  LR at 50,029.5 km, just 3 km outside the ring. As such, it could readily explain both of the ring's mysterious properties.

The amplitude of the radial distortion is proportional to the mass  $M_s$  of the unseen moon, by a relation that can be derived by combining equations 16 and 17 in (17). A pattern amplitude of  $4.2 \pm 0.9$  km requires  $M_s = (1.0 \pm 0.2) \times 10^{20}$  g. This mass then implies a limit on the moon's orbital eccentricity  $e_s$  that is needed for the CR to maintain libration in the ring (18). For a ring 2 km wide,  $e_s > 1.5 \times 10^{-3}$ , which is com-

**Fig. 2.** A complete set of equivalent width measurements for the  $\lambda$  ring from the Voyager images. Vertical error bars indicate  $\pm 1\sigma$  based on the statistical properties of each profile combined with the systematic uncertainty in its baseline. Horizontal bars indicate the range of longitudes averaged together for each point. Measurements are plotted as a function of longitude in a frame corotating with the ring material, converted to the nominal time of Voyager's closest approach to Uranus (17:59:00 UTC on 24 January 1986); longitude  $0^\circ$  corresponds to the ascending node of the ring plane on Earth's mean equator of 1950 (EME50). The open circles indicate measurements from the inbound sequence of images 26813.28 to 26824.20, which have phase angles  $\alpha = 17^\circ$  to  $21^\circ$ ; filled circles are from the outbound image sequence 26871.51 to 26881.56, where  $\alpha = 149^\circ$  to  $152^\circ$ . In both sequences, the radial resolution is  $\sim 10$  km/pixel. The inbound data have been scaled by a factor of 1.5 to accommodate the ring's phase curve (12). An overall 5-cycle periodicity is visible.

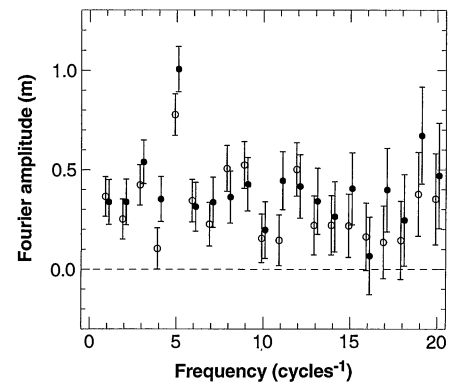
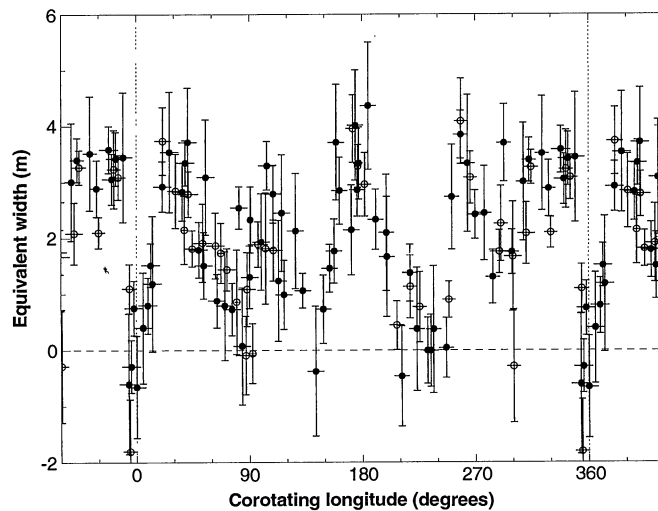


**Fig. 3.** Coefficients for a Fourier series generated from the measurements shown in Fig. 2. The values plotted are amplitudes only; that is,  $\sqrt{a_k^2 + b_k^2}$ , where  $a_k$  are the cosine coefficients and  $b_k$  are the sine coefficients. Error bars indicate  $\pm 1\sigma$ . Two different methods have been used to determine the Fourier coefficients: (i) filled circles indicate a simultaneous linear least squares fit to the data using a constant and the first 20 sine and cosine harmonics; (ii) open circles indicate a series based on successively fitting each harmonic  $k$  to the data, subtracting it, and then fitting the next harmonic to the residuals. The two methods would be equivalent if the data were uniformly spaced and equally weighted, but method (i) can be very unstable for sparse data. Regardless of the method, the  $k = 5$  harmonic clearly stands out above the others. The constant term is off of the scale at  $\sim 4$  m.

parable to the eccentricities of the known inner Uranian moons (5). Unfortunately, the mass requirement implies that Voyager should have detected the moon; assuming a density  $\rho = 1.5 \text{ g/cm}^3$ , the moon would have a radius  $R_s = 54 \pm 4 \text{ km}$ . For comparison, the moons discovered during the Uranus encounter have  $R_s = 13$  to  $77 \text{ km}$  (19). Smith *et al.* (1) claim that no body with  $R_s > 10 \text{ km}$  could have escaped detection.

The one moon that we do know about near the  $\lambda$  ring is Cordelia. Cordelia's  $m = 121$  CER falls at  $50,027.0 \pm 0.3 \text{ km}$ , which is marginally compatible with the ring's semimajor axis inferred above,  $50,026.3 \pm 0.6 \text{ km}$ . However, this association may be purely coincidental because Cordelia's resonances are spaced by only  $2.3 \text{ km}$  in the vicinity. Cordelia's eccentricity and radius

are highly uncertain:  $e_s = (4.7 \pm 4.1) \times 10^{-4}$  (5) and  $R_s = 13 \pm 2 \text{ km}$  (19); its density is unconstrained. However, assuming the quoted mean values and  $\rho = 1.5 \text{ g/cm}^3$ , Cordelia is able to maintain libration within a ring  $\sim 0.6 \text{ km}$  wide (18). This is smaller than the ring's full  $2\text{-km}$  width, but it is comparable to the  $0.5\text{-km}$  core detected by the PPS. This might suggest a ring model with two components: a core containing large longitudinal variations surrounded by a fainter and more uniform "skirt." The PPS data generally support this model because the broader skirt appears in both occultation cuts but the core is especially prominent at egress [see figure 3 in (2)]. Although Cordelia's CER cannot explain the ring's dominant brightness periodicity, it could stabilize variations by preventing particles

from passing between libration sites  $2.98^\circ$  apart. The  $0.5^\circ$  clump (Fig. 4) may be confined by one of these sites.

Perhaps a combination of resonances by Cordelia plus a smaller version of the hypothesized moon can provide a more complete explanation. The unseen moon's  $m = 5$  CER falls near the  $\lambda$  ring and modulates the pattern of five arcs, but Cordelia's CER is primarily responsible for arc confinement. The moon must still drive the observed radial mode. However, if the ring is displaced closer to the moon's LR (and therefore further from its CER), then a smaller  $M_s$  can produce the same amplitude. Alternatively, ring self-gravity can sustain or amplify radial modes (20), such as those in the  $\gamma$  and  $\delta$  rings. Future photometry may settle the question of whether the  $\lambda$  ring contains sufficient mass to amplify a radial mode driven by a nearby LR (12).

The closest known analog to this dynamical system is Neptune's Adams ring with Galatea. Galatea's  $m = 43$  CIR falls atop the ring and appears to confine the arcs (13), while its  $m = 42$  LR drives a radial pattern in the ring. Like the  $\lambda$  ring, this ring also presents a significant challenge to current theories: Galatea's mass is  $1/25$  of that needed to confine the observed arcs. Proposed explanations for the discrepancy (21) remain controversial.

Reanalysis of Earth-based occultation data may provide more insight into the  $\lambda$  ring's kinematics. Previous nondetections have been based on the assumption that the ring is uniform and circular. In light of the results presented here, observers would do well to review old data and take note of any feature between  $50,019$  and  $50,033 \text{ km}$ . With additional detections, it may be possible to reconstruct the ring's kinematics with much greater accuracy.

The  $\lambda$  ring is now known to be one of only a few planetary rings containing longitudinal variations and the only one for which a single periodicity dominates. It shares several key traits with the Adams ring and poses similar difficulties for current dynamical models. Further studies may reveal whether common dynamical processes are at work.

## REFERENCES AND NOTES

1. B. A. Smith *et al.*, *Science* **233**, 43 (1986).
2. J. E. Colwell *et al.*, *Icarus* **83**, 102 (1990).
3. J. B. Holberg, P. D. Nicholson, R. G. French, J. L. Elliot, *Astron. J.* **94**, 178 (1987).
4. R. G. French, P. D. Nicholson, C. C. Porco, E. A. Marouf, in *Uranus*, J. T. Bergstrahl, E. D. Miner, M. S. Matthews, Eds. (Univ. of Arizona Press, Tucson, 1991), pp. 327–409.
5. W. M. Owen Jr. and S. P. Synnott, *Astron. J.* **93**, 1268 (1987).
6. D. L. Gresh *et al.*, *Icarus* **78**, 131 (1989).
7. J. A. Kangas and J. L. Elliot, *Bull. Am. Astron. Soc.* **19**, 884 (1987).
8. R. G. French *et al.*, *ibid.* **25**, 1111 (1993).

**Fig. 4.** Voyager image 26852.14, a 1.92-s exposure, shows a clump  $\sim 0.5^\circ$  long in the  $\lambda$  ring; the other rings are invisible. The clump falls at longitude  $99^\circ$  in the rotating frame. For comparison, a strip from the much better known 96-s exposure that followed it, 28652.19, is shown at the right, aligned appropriately; this image shows the main rings plus additional dust belts but is too badly smeared to show the clump.

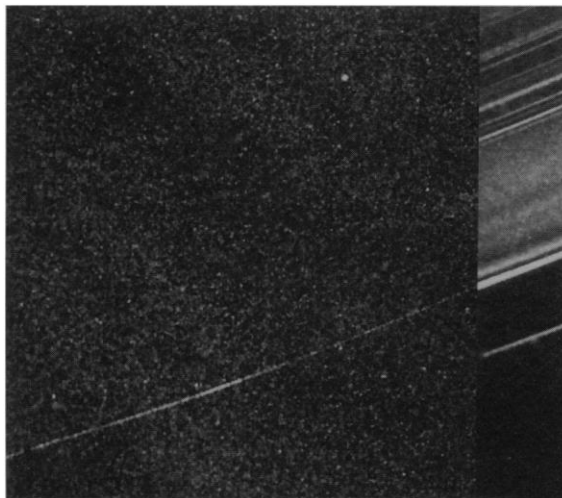
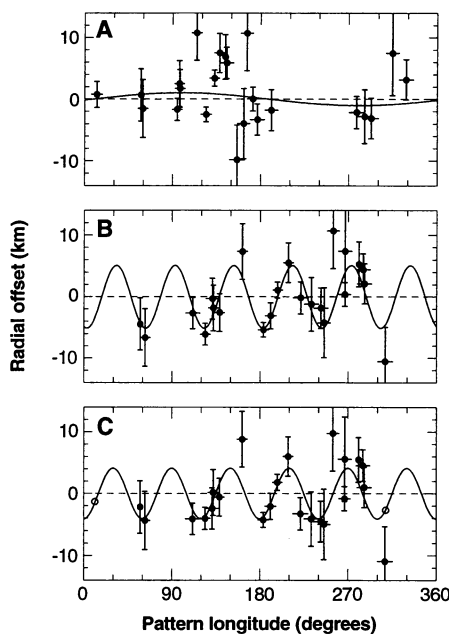


**Fig. 5.** Residuals to models of the  $\lambda$  ring's shape. Measurements are shown only for inbound images in which the ring was easily detected. Vertical error bars are  $\pm 1\sigma$ , based on the overall uncertainty in the radial scale combined with the formal uncertainty in the estimate of the  $\lambda$  ring's midpoint. Rings  $\alpha$ ,  $\beta$ ,  $\gamma$ ,  $\delta$ , and  $\epsilon$  have been used for the radial reference, with the best shape models available (4). Horizontal bars indicate the range of longitudes averaged. Longitude  $0^\circ$  corresponds to the ascending node of the ring plane in EME50 at the time of Voyager's closest approach. (A) Residuals from the semimajor axis for an ellipse fit. Longitudes are measured in a frame rotating at the ring's apsidal precession rate derived from the gravity model (4). The curve indicates the best-fit eccentricity, which is a very poor fit to the data. The "goodness of fit"  $G \equiv \sqrt{\chi^2/N}$  is the root-mean-square deviation of the points from the curve in units of  $\sigma$ , where  $N$  is the number of degrees of freedom. We expect that  $G \approx 1$  for a good fit to the data, but  $G = 1.47$  here. (B) Residuals from the best-fit ellipse after a simultaneous fit to an  $m = 6$  radial mode. Longitudes are measured in a frame rotating at the mode's predicted pattern speed. The curve shows the derived  $m = 6$  pattern, which represents an excellent fit to the data ( $G = 0.97$ ). (C) Same as (B), but with the two PPS detections (open circles) also included in the fit. The fit is still acceptable ( $G = 1.09$ ).



9. M. R. Showalter, J. N. Cuzzi, S. M. Larson, *Icarus* **94**, 451 (1991).
10. M. R. Showalter and J. N. Cuzzi, *ibid.* **103**, 124 (1993).
11. M. R. Showalter, *Bull. Am. Astron. Soc.* **23**, 1178 (1991).
12. ———, *ibid.* **25**, 1109 (1993).
13. C. C. Porco, *Science* **253**, 995 (1991).
14. M. E. Ockert, J. N. Cuzzi, C. C. Porco, T. V. Johnson, *J. Geophys. Res.* **92**, 14969 (1987).
15. B. A. Smith *et al.*, *Science* **212**, 163 (1981).
16. M. R. Showalter, *Nature* **351**, 709 (1991).
17. P. Goldreich, S. Tremaine, N. Borderies, *Astron. J.* **92**, 490 (1986).
18. B. Sicardy, *Icarus* **89**, 197 (1991).
19. P. Thomas, C. Weitz, J. Veverka, *ibid.* **81**, 92 (1989).
20. P.-Y. Longaretti, *ibid.* **82**, 281 (1989).
21. C. C. Porco, P. D. Nicholson, J. N. Cuzzi, J. J. Lisauer, L. W. Esposito, in *Neptune and Triton*, D. P. Cruikshank, Ed. (Univ. of Arizona Press, Tucson, in press).
22. The processing behind the profiles involves (i) correcting the camera orientation on the basis of the observed locations of background stars (and allowing for stellar aberration in the frame of the planet); (ii) masking out all invalid pixels, such as those containing stars, satellites, blemishes in the camera vidicon, or reseau markings; (iii) converting the image to a one-dimensional profile by averaging together all unmasked pixels falling at the same radius but different longitudes; and (iv) removing residual background variations by fitting a low-order polynomial to the samples outside the ring's radial limits and subtracting it. These procedures are described elsewhere (9, 10). Note that step (iii) substantially increases the detectability of faint rings; a narrow ring typically occupies ~800 pixels in a Voyager image, so this averaging improves the signal-to-noise ratio by a factor of  $\sqrt{800} \approx 30$ .
23. I thank the Voyager Imaging and PPS teams and the Planetary Data System Imaging Node for providing the data. I am indebted to A. Dobrovolskis, L. Dones, R. French, B. Sicardy, and two anonymous referees for helpful comments and criticisms. This work was supported by the National Aeronautical and Space Administration (NASA) Planetary Geology and Geophysics program and by NASA Ames under grant NAG2-673.

26 July 1994; accepted 25 October 1994

## Energy Dependence of Abstractive Versus Dissociative Chemisorption of Fluorine Molecules on the Silicon (111)-(7×7) Surface

John A. Jensen, Chun Yan, Andrew C. Kummel\*

Scanning tunneling microscopy and monoenergetic molecular beams have been used to obtain real-space atomic images of the competition between abstractive and dissociative chemisorption. The size distribution of Si-F adsorbates on the Si(111)-(7×7) surface was examined as a function of the incident translational energy of the F<sub>2</sub> molecules. For F<sub>2</sub> molecules with 0.03 electron volt of incident energy, the dominant adsorbate sites were isolated Si-F species. As an F<sub>2</sub> molecule with low translational energy collides with the surface, abstraction occurs and only one of the F atoms chemisorbs; the other is ejected into the gas phase. For F<sub>2</sub> molecules with 0.27 electron volt of incident energy, many adjacent Si-F adsorbates (dimer sites) were observed because F<sub>2</sub> molecules with high translational energy collide with the surface and chemisorb dissociatively so that both F atoms react to form adjacent Si-F adsorbates. For halogens with very high incident energy (0.5–electron volt Br<sub>2</sub>), dissociative chemisorption is the dominant adsorption mechanism and dimer sites account for nearly all adsorbates.

The chemisorption of F<sub>2</sub> is often the first step in the dry etching of Si. For most molecules, chemisorption on surfaces occurs either through a physisorbed precursor state or by direct chemisorption (1). Dissociative chemisorption is a common gas-surface process in which an incident molecule collides with the surface and breaks apart to form two or more chemisorbates. For dissociative chemisorption of F<sub>2</sub> on Si, direct chemisorption is so highly exothermic that a distinct mechanism can occur. In abstractive chemisorption, as an incident F<sub>2</sub> collides with the surface, one F atom is chemisorbed onto a Si atom and the terminal F atom is ejected into the gas phase. Molecular beam scattering experiments by Ceyer and co-

workers (2) have demonstrated the existence of abstractive chemisorption for F<sub>2</sub> on the Si(100)-(2×1) surface; to our knowledge, this is the only experimental report of abstractive chemisorption of any molecule onto a surface. Molecular dynamics simulations by Carter *et al.* (3) have shown that this abstraction mechanism is most efficient at low translational energy, whereas dissociative chemisorption is most efficient at high translational energies. They have also shown that the reaction of F<sub>2</sub> with the Si(100)-(2×1) surface always proceeds in a stepwise fashion, the first step being the chemisorption of one F atom and the cleavage of the F-F bond. The escape or adsorption of the second F atom is the difference between abstractive and dissociative chemisorption.

In this report, we present atomic-resolution scanning tunneling microscopy (STM)

images of the Si(111)-(7×7) surface after chemisorption of F<sub>2</sub> molecules with low and high translational energies. These images allow direct observation of how the probability for abstraction varies with the incident translational energy of F<sub>2</sub> in the limit of zero coverage. We show that for F<sub>2</sub> molecules with low incident translational energy, nearly all chemisorption sites are Si-F monomers, that is, isolated single sites formed through abstractive chemisorption. We also show that for F<sub>2</sub> molecules with higher incident translational energy, many more chemisorption sites are dimers, that is, two nearest neighbor Si-F sites formed through dissociative chemisorption. Finally, for Br<sub>2</sub> molecules with very high incident translational energy, dissociative chemisorption accounts for essentially all adsorption because single-site adsorbates are almost absent. Our experiments show that the competition between abstractive and dissociative chemisorption is mediated by the incident translational energy and momentum of the molecule.

Both molecular beam techniques and STM are required to examine the initial stages of F<sub>2</sub> adsorption onto the Si(111)-(7×7) surface. The supersonic expansion of the halogen-carrier gas mixture provides a source of halogen molecules with a very narrow translational energy distribution ( $\Delta E/E \leq 2\%$ ) as well as a low rotational temperature (~4 K). By changing the mixture ratio or mass of the carrier gas, it is possible to vary the translational energy of the halogen without changing the rotational or vibrational temperature of the molecules. The STM allows us to examine the resulting adsorbate structures with atomic resolution.

Earlier experiments and calculations (2, 3) characterizing the abstraction mechanism were carried out on the dimer row Si(100)-(2×1) surface. In our study we used the Si(111)-(7×7) surface. The structure of the Si(111)-(7×7) unit cell is well known (4) (Fig. 1). Only the adatoms (first layer) and those rest atoms (second layer) with dangling bonds are shown in Fig. 1; these are the surface atoms that do not have complete coordination of four neighboring Si atoms and thus have localized electron density that is centered along the missing bond axis. This localized electron density is termed a dangling bond. Empty-state STM images show only the adatom dangling bonds (the 12 uppermost Si atoms shown as open circles inside the border in Fig. 1). Empty-state images do not show the rest atom dangling bonds located one atomic layer below (the six atoms shown as crossed circles in Fig. 1). It has been shown experimentally (5) and theoretically (6) that each adatom dangling bond has an occupancy of approximately one-half an elec-

Department of Chemistry, 0358, University of California, San Diego, 9500 Gilman Drive, La Jolla, CA 92093, USA.

\*To whom correspondence should be addressed.